The effect of the point spread function on sub-pixel mapping

Qunming Wang [a], Peter M. Atkinson [a,b,c,*]

[a] Lancaster Environment Centre, Lancaster University, Lancaster LA1 4YQ, UK

[b] Geography and Environment, University of Southampton, Highfield, Southampton SO17 1BJ, UK

[c] School of Geography, Archaeology and Palaeoecology, Queen's University Belfast, BT7 1NN, Northern Ireland, UK

*Corresponding author

E-mail: pma@lancaster.ac.uk

Abstract: Sub-pixel mapping (SPM) is a process for predicting spatially the land cover classes within mixed pixels. In existing SPM methods, the effect of point spread function (PSF) has seldom been considered. In this paper, a generic SPM method is developed to consider the PSF effect in SPM and, thereby, to increase prediction accuracy. We first demonstrate that the spectral unmixing predictions (i.e., coarse land cover proportions used as input for SPM) are a convolution of not only sub-pixels within the coarse pixel, but also sub-pixels from neighboring coarse pixels. Based on this finding, a new SPM method based on optimization is developed which recognizes the optimal solution as the one that when convolved with the PSF, is the same as the input coarse land cover proportion. Experimental results on three separate datasets show that the SPM accuracy can be increased by considering the PSF effect.

1. Introduction

Mixed pixels are inevitable in remote sensing images and have brought great challenges in land cover mapping. The spectral unmixing technique has been studied for decades to estimate the proportions of land cover classes within mixed pixels (Bioucas-Dias et al., 2012; Heinz & Chang, 2001; Keshava & Mustard, 2002). The proportions are at the same spatial resolution as the input images and cannot inform the spatial distribution of classes within mixed pixels. To further estimate the spatial distribution of land cover, sub-pixel mapping (SPM) was developed as a post-processing analysis of spectral unmixing outputs. SPM divides mixed pixels to sub-pixels and predicts their class attributes under the coherence constraint from prior spectral unmixing predictions (i.e., coarse land cover class proportions). SPM transforms the conventional pixel-level classification to a finer spatial resolution hard classification (Atkinson, 1997), which can provide more explicit thematic information (e.g., the boundaries between land cover classes can be characterized by more pixels).

In recent decades, various SPM approaches have been developed. As a post-processing step of spectral unmixing, two main groups of SPM approaches can be identified. The first group considers the relation between sub-pixels and solutions are always produced based on defined objectives. Based on the assumption of spatial dependence, the objective can be determined empirically as maximizing the spatial attraction between sub-pixels (Makido & Shortridge, 2007), maximizing the Moran's I (Makido et al., 2007) or minimizing the perimeter of the area for each class (Villa et al., 2011). Based on prior knowledge, the objective can also be matching prior patterns extracted from training images, such as characterized by the semivariogram (Tatem et al., 2002), two-point histogram (Atkinson, 2008) or landscape structure (Lin et al., 2011). The SPM solutions of this type of methods are achieved based on optimization, including the Hopfield neural network (HNN) (Ling et al., 2010; Muad & Foody, 2012; Nguyen et al., 2011; Tatem et al., 2001), pixel swapping algorithm (PSA) (Atkinson, 2005; Shen et al., 2009; Xu & Huang, 2014), maximum *a posteriori* method (Zhong et al., 2015), genetic algorithm (Li et al., 2015; Mertens et al., 2003; Tong et al., 2016), and particle swarm optimization (PSO) (Wang et al., 2012). Several iterations are involved for this group of SPM methods and,

51 thus, a relatively long computing time may be required. The second group of SPM methods considers the

52 relation between sub-pixels and neighboring pixels. The coarse class proportions within each pixel are used

53 directly to characterize the relation between it and sub-pixels and calculate the fine spatial resolution

54 proportions for sub-pixels. Under the coherence constraint, the sub-pixel classes are determined by comparing

55 the fine spatial resolution proportions. As the coarse proportions are fixed for a given pixel, iterations (as in the

56 first method type) are not necessarily involved and SPM solutions can be produced more quickly. Methods

57 falling into this type include sub-pixel/pixel spatial attraction model (SPSAM) (Mahmood et al., 2013; Mertens

58 et al., 2006; Xu et al., 2014), back-propagation neural network-based algorithm (Gu et al., 2008; Zhang et al.,

59 2008), learning-based algorithm (Zhang et al., 2014), kriging (Verhoeye & Wulf, 2002; Boucher & Kyriakidis,

60 2006) and radial basis function (RBF) (Wang et al., 2014a) interpolation. They can also be summarized as the

61 soft-then-hard SPM (STHSPM) algorithms, a concept proposed in our previous work (Wang et al., 2014b;

62 Chen et al., 2015). In addition, to reduce the uncertainty introduced by spectral unmixing, some SPM methods

63 that do not rely absolutely on coarse proportions were developed, including spatial-spectral methods (Ardila et

64 al., 2011; Kasetkasem et al., 2005; Li et al., 2014; Tolpekin & Stein, 2009), spatial regularization (Ling et al.,

65 2014; Zhang et al., 2015) and contouring methods (Foody & Doan, 2007; Ge et al., 2014; Su et al., 2012).

66 In remote sensing images, the point spread function (PSF) effect exists ubiquitously. It means that the signal

67 for a given pixel is a weighted combination of contributions from within the pixel and also contributions from

68 neighboring pixels (Townshend et al., 2000; Van der Meer, 2012). The PSF can brighten dark objects and

69 darken bright objects observed from the surface (Huang et al., 2002). It results in a fundamental limit on the

70 amount of information that remote sensing images can contain (Manslow & Nixon, 2002). The PSF is a

71 two-dimensional function accounting for both the across-track and along-track directions (Campagnolo &

72 Montano, 2014; Radoux et al., 2016). The PSF effect is caused mainly by the optics of the instrument, the

73 detector and electronics, atmospheric effects, and image resampling (Huang et al., 2002; Schowengerdt, 1997).

74 The PSF effect may not be an important issue for homogeneous regions, but it is crucial for heterogeneous

75 landscapes dominated by mixed pixels. To the best of our knowledge, very few SPM methods have considered

the PSF effect in downscaling. For example, in most of the existing SPM methods, the coherence constraint from class proportions is satisfied simply by fixing the number of sub-pixels for each class within a single coarse pixel (i.e., the ideal square wave PSF is considered). The number of sub-pixels to be allocated to a class within a coarse pixel is calculated as the product of the coarse class proportion within the coarse pixel and the square of the zoom factor. Due to the PSF effect, however, the coarse proportions estimated by spectral unmixing are actually a function, in part, of the neighboring coarse pixels. The uncertainty in coarse proportions is propagated to the post-SPM process where the coarse proportions contaminated by neighboring coarse pixels are used as the coherence constraint. There is, therefore, a great need for an approach accounting for the PSF effect in SPM to increase the prediction accuracy.

There are two plausible solutions to cope with the PSF effect in SPM. One is to consider the PSF effect in the pre-spectral unmixing process and to estimate more reliable coarse proportions from observed multispectral images. Based on the more reliable predictions, the PSF need not be considered in SPM (i.e., the ideal square wave PSF can be considered in SPM, as in existing SPM approaches). However, spectral unmixing is an ill-posed inverse problem. It is more complicated when part of the neighboring coarse pixels (i.e., neighboring sub-pixels) are involved as this technique is generally performed at the pixel resolution. Currently, it is challenging to account for the PSF in spectral unmixing and obtain reliable proportions. The alternative solution, considered here, is to model the PSF effect in the SPM process, based on the proportions contaminated by neighboring coarse pixels. This strategy is more feasible as SPM is conducted at the sub-pixel scale and contributions from neighboring sub-pixels in PSF can be straightforwardly modeled.

In this paper, to increase the SPM accuracy, the PSF effect is considered directly in the SPM process. Most SPM methods need to first calculate the number of sub-pixels for each class within each coarse pixel. Based on these fixed numbers, the sub-pixel classes are then predicted. This is not a problem for the ideal square wave PSF, as mentioned earlier. When considering the non-ideal PSF, however, the coarse proportions are a convolution of the sub-pixel class values in a larger local window, rather than the single coarse pixel in the ideal square-wave PSF. In this case, the number of sub-pixels for each class in each coarse pixel cannot be

101 determined using only the single coarse proportion (i.e., product of the coarse proportion and the square of the

102 zoom factor, as in existing SPM methods), and it actually cannot be calculated explicitly. In this case, SPM

103 methods such as the STHSPM algorithms are not suitable choices. A plausible solution to this issue is to

104 convolve the fine spatial resolution SPM realization with the PSF and compare the estimated proportion with

105 the actual coarse proportion, and use the error to guide further updating of the current realization. The

106 iteration-based HNN is a method of this type. Therefore, in this paper, the HNN is used to reduce the

107 uncertainty in SPM introduced by the PSF effect.

108 The remainder of this paper is organized into four sections. Section 2 first introduces the mechanism of the

109 PSF effect in SPM and then the details of the proposed strategy for considering the PSF in SPM. The

110 experimental results for three groups of datasets are provided in Section 3 for validation of the proposed

111 method. Section 4 further discusses the proposed SPM method, followed by a conclusion in Section 5.

112

113

114 **2. Methods**

115

116 *2.1. The PSF effect in SPM*

117 This section will illustrate the PSF effect in SPM and demonstrate that the coarse proportions in SPM are a

118 convolution of the sub-pixel class values in a local window centered at the coarse pixel. Let $\mathbf{S}_V$ be the spectrum

119 of coarse pixel V, $\mathbf{R}_k$ be the spectrum of class endmember k (k=1, 2, …, K, where K is the number of land

120 cover classes), and $F_k(V)$ be the proportion of class k in pixel V. Based on the classical linear spectral mixture

121 model (Bioucas-Dias et al., 2012; Heinz & Chang, 2001; Keshava & Mustard, 2002), the spectrum of each

122 coarse pixel is a linear combination of the spectrum of endmembers, where the weights are determined as the

123 class proportions within the coarse pixel. That is

124
$$\mathbf{S}_V = \sum_{k=1}^{K} \mathbf{R}_k F_k(V).$$
(1)

125 Due to the PSF effect in remote sensing images, Eq. (2) holds

$$\mathbf{S}_V = \mathbf{S}_v * h_V \tag{2}$$

127 where $\mathbf{S}_v$ is the spectrum of sub-pixel v, h_V is the PSF and $*$ is the convolution operator. For sub-pixel v, its

128 spectrum $\mathbf{S}_v$ can be characterized as

$$\mathbf{S}_v = \sum_{k=1}^{K} \mathbf{R}_k I_k(v) \tag{3}$$

130 in which $I_k(v)$ is a class indicator as follows

$$I_k(v) = \begin{cases} 1, & \text{if sub-pixel } v \text{ belongs to class } k \\ 0, & \text{otherwise} \end{cases}. \tag{4}$$

132 By substituting Eq. (3) into Eq. (2), we have

$$\mathbf{S}_V = \left[\sum_{k=1}^{K} \mathbf{R}_k I_k(v) \right] * h_V = \sum_{k=1}^{K} \mathbf{R}_k \left[I_k(v) * h_V \right]. \tag{5}$$

134 The comparison between Eq. (1) and Eq. (5) leads to

$$F_k(V) = I_k(v) * h_V. \tag{6}$$

136 Let z be the zoom factor, that is, each coarse pixel is divided into z by z sub-pixels. As shown in the one

137 dimensional illustration in Fig. 1, when the PSF takes the ideal square wave filter in Eq. (7)

$$h_V(i, j) = \begin{cases} \dfrac{1}{z^2}, & \text{if } (i, j) \in V(i, j) \\ 0, & \text{otherwise} \end{cases} \tag{7}$$

139 where (i, j) is the spatial location of the sub-pixel and $V(i, j)$ is the spatial extent of the coarse pixel V

140 containing the sub-pixel at (i, j). Further, the convolution in Eq. (6) can be simplified as

$$F_k(V) = \frac{\displaystyle\sum_{i,j=1}^{z} I_k(v_{ij})}{z^2}. \tag{8}$$

142 In Eq. (8), all sub-pixels v_{ij} are located within coarse pixel V. This means that based on the assumption of an

143 ideal square wave PSF, the coarse class proportion estimated from the linear spectral mixture model in Eq. (1)

144 is viewed as the average of all sub-pixel class indictors within the pixel. This is the common case considered in

145 most SPM methods.

146
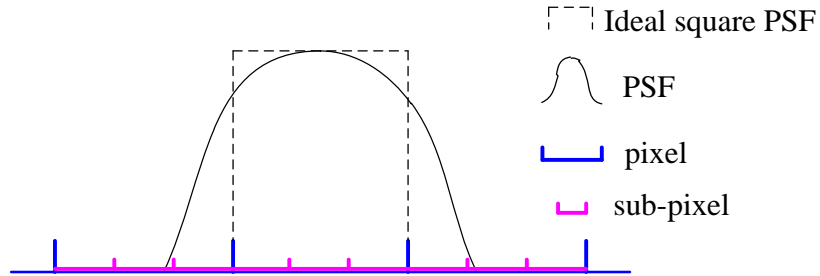
148 Fig. 1 A one dimensional illustration of the PSF in SPM. Based on the real PSF, the coarse pixel value (or coarse class proportion)

149 should be a convolution of the sub-pixel values (or sub-pixel class indicators) located within the local window centered at the coarse

150 pixel, rather than only within the single coarse pixel (as assumed in the ideal square wave PSF).

151

152 In reality, the PSF is different to the ideal square wave filter. The spatial coverage of h_v is generally larger

153 than a coarse pixel size, but is finite, as shown in Fig. 1. For example, the PSF can be the Gaussian filter, which

154 is used widely in remote sensing (Campagnolo & Montano, 2014; Huang et al., 2002; Manslow & Nixon, 2002;

155 Townshend et al., 2000; Van der Meer, 2012; Wenny et al., 2015)

$$h_V(i, j) = \begin{cases} \dfrac{1}{2\pi\sigma^2} \exp\left[-\left(\dfrac{i^2 + j^2}{2\sigma^2}\right)\right], & \text{if } (i, j) \in V'(i, j) \\ 0, & \text{otherwise} \end{cases} \tag{9}$$

157 where σ is the standard deviation (width of the Gaussian PSF) and $V'(i, j)$ is the spatial extent of the local

158 window centered at coarse pixel V (V covers the sub-pixel at (i, j)), see Fig. 1. Thus, any sub-pixel v involved in

159 the calculations in Eq. (2) and Eq. (6) falls within a wider spatial coverage $V'(i, j)$, rather than only within

160 $V(i, j)$. This means that based on the linear spectral mixture model in Eq. (1), the estimated coarse class

161 proportions within each coarse pixel are actually a convolution of the sub-pixels in the local window centered

162 at the coarse pixel, rather than only the sub-pixels within the coarse pixel (i.e., not the case in Eq. (8)).

163

164

165   *2.2. Enhancing SPM by considering the PSF effect*

166   In conventional SPM, the number of sub-pixels for each class needs to be determined in advance, which is

167   used as a coherence constraint in the mapping process. Let $N_k(V)$ be the number of sub-pixels for class k in

168   pixel *V*, which is usually calculated as

$$N_k(V) = \text{round}\left[F_k(V) \times z^2 \right]. \tag{10}$$

170   From Section 2.1, it is concluded that in reality the estimated coarse proportions are contaminated by their

171   neighboring pixels due to the PSF effect (see Eq. (6)). Therefore, it is generally incorrect to use Eq. (10) for the

172   coherence constraint in SPM, unless the correct land cover proportions (i.e., not contaminated by neighbors)

173   can be produced. As can be seen from Eq. (5), even when the endmember set $\mathbf{R}_k$ and PSF h_V are known

174   perfectly, it is not trivial to determine the correct proportions. This is because the coarse proportions can

175   sometimes be functions of neighboring sub-pixels, as can be seen from Eq. (6) and Fig. 1. In this case where

176   sub-pixels are involved, spectral unmixing becomes challenging, as unmixing is carried out at the pixel

177   resolution and cannot account for proportions at the sub-pixel resolution. Townshend et al. (2000) and Huang

178   et al. (2002) proposed an interesting deconvolution method to reduce the impact of the PSF in coarse

179   proportion predictions. This method was developed at the pixel resolution, which quantifies the contributions

180   from neighbors in units of coarse pixels. That is, it treats all sub-pixels in a surrounding coarse pixel equally

181   and assumes a uniform contribution to the center coarse pixel. According to Fig. 1, however, sub-pixels in the

182   surrounding coarse pixel have a different spatial distance to the center coarse pixel and thus, should have

183   different contributions to the center coarse proportion (e.g., some sub-pixels even have no contribution).

184   In this paper, the coarse proportions contaminated by pixel neighbors are directly considered in SPM. As

185    $N_k(V)$ cannot be calculated explicitly, conventional SPM methods such as the STHSPM algorithms cannot be

186   used. Guided by the mechanism in Eq. (6), the ideal SPM solution should be the one that when convolved with

187   the PSF, is the same as the coarse proportion. Alternatively, an optimization-based SPM method is employed in

188   this paper, where the convolution of the current SPM realization is compared with the contaminated coarse

189 proportions for updating SPM predictions iteratively. The HNN is a method suitable for this task and is used for

190 accounting for the PSF in SPM. The HNN has been used widely in SPM, appreciating its highly satisfactory

191 performance (Ling et al., 2010; Muad & Foody, 2012; Nguyen et al., 2011; Tatem et al., 2001). It considers

192 each sub-pixel as a neuron and works by minimizing an energy function composed of a goal and a coherence

193 constraint term. The HNN accounting for the PSF effect is introduced below.

194 Suppose (k, i, j) is a neuron for sub-pixel at location (i, j) and is on the network layer representing land cover

195 class k, and q_{kij} is its output. If q_{kij} is 1, it means that the sub-pixel at (i, j) is belongs to class k, and if q_{kij} is 0,

196 the sub-pixel does not belong to class k. Using the HNN, the outputs are update iteratively for each sub-pixel.

197 The output q_{kij} is a function of the input signal u_{kij}

198
$$q_{kij} = \frac{1}{2}\left[1 + \tanh\left(\lambda u_{kij}\right)\right] \tag{11}$$

199 where λ determines the steepness of the function. The input u_{kij} for the t-th iteration is updated by

200
$$u_{kij}\left(t + dt\right) = u_{kij} + \frac{du_{kij}\left(t\right)}{dt} dt \tag{12}$$

201 in which dt is a time step. The second term on the right hand side of Eq. (12) is the energy change of the

202 neuron and is described as

203
$$\frac{du_{kij}\left(t\right)}{dt} = -\frac{dE_{kij}}{dq_{kij}}. \tag{13}$$

204 In Eq. (13), E represents the network energy function and is described as

205
$$E = \sum_k \sum_i \sum_j \left(w_1 G1_{kij} + w_2 G2_{kij} + w_3 P_{kij} + w_4 M_{kij}\right) \tag{14}$$

206 where w_1, w_2, w_3 and w_4 are four weights, $G1$ and $G2$ are two spatial clustering functions characterizing

207 spatial dependence, P is the proportion constraint and M is the multi-class constraint (Ling et al., 2010; Nguyen

208 et al., 2011). Accordingly, the energy change of the neuron for sub-pixel at (i, j) in Eq. (13) is determined by

209
$$\frac{dE_{kij}}{dq_{kij}} = w_1 \frac{dG1_{kij}}{dq_{kij}} + w_2 \frac{dG2_{kij}}{dq_{kij}} + w_3 \frac{dP_{kij}}{dq_{kij}} + w_4 \frac{dM_{kij}}{dq_{kij}}. \tag{15}$$

The first two terms of the right hand side of Eq. (15) are calculated as

$$\frac{dG1_{kij}}{dq_{kij}} = \frac{1}{2}\left[1 + \tanh\left(\frac{1}{8}\left(\sum_{b=i-1}^{i+1}\sum_{c=j-1}^{i+1} q_{kbc} - q_{kij}\right) - 0.5\right)\lambda\right](q_{kij} - 1) \tag{16}$$

$$\frac{dG2_{kij}}{dq_{kij}} = \frac{1}{2}\left[1 - \tanh\left(\frac{1}{8}\left(\sum_{b=i-1}^{i+1}\sum_{c=j-1}^{i+1} q_{kbc} - q_{kij}\right) - 0.5\right)\lambda\right]q_{kij}. \tag{17}$$

If the average output of the surrounding neurons is larger than 0.5, the function $G1$ increases the neuron output to approach 1 to increase the spatial correlation between neighboring sub-pixels. Otherwise, if the average output of the surrounding neurons is less than 0.5, the function $G2$ decreases the neuron output to 0.

The multi-class constraint means that for any sub-pixel, the sum of neuron outputs for all K classes should be equal to 1, thus

$$\frac{dM_{kij}}{dq_{kij}} = \left(\sum_{n=1}^{K} q_{nij}\right) - 1. \tag{18}$$

Considering the PSF effect, the proportion constraint for class k is expressed as

$$\frac{dP_{kij}}{dq_{kij}} = L_k(V_{ij}) - F_k(V_{ij}) \tag{19}$$

where V_{ij} is the coarse pixel that sub-pixel at (i, j) falls within, $F_k(V_{ij})$ is the target coarse proportion of class k in the pixel (i.e., spectral unmixing predictions), and $L_k(V_{ij})$ is the coarse proportion estimated as convolution of the current SPM realization. Based on the mechanism in Eq. (6), $L_k(V_{ij})$ is calculated as

$$L_k(V_{ij}) = \frac{1}{2}\left[1 + \tanh\left(q_k - 0.5\right)\lambda\right] * h_V$$
$$= \iint_{(x,y)\in V'(i,j)} \frac{1}{2}\left[1 + \tanh\left(q_k - 0.5\right)\lambda\right]h_V(x - i_0, y - j_0)d_x d_y \tag{20}$$

in which $V'(i, j)$ is defined in the same way as that in Eq. (9) and (i_0, j_0) is the spatial location of the center of coarse pixel V_{ij}. The *tanh* function is used in Eq. (20) to ensure that if the neuron output q_k is above 0.5, it is counted as an output of 1 (i.e., belongs to class k) for the coarse proportion calculation; If q_k is below 0.5, it is

228 not counted for class k instead. This ensures that the neuron output exceeds 0.5 in order to be counted within the

229 calculations for each class.

230 In Eq. (19), the target coarse proportion $F_k(V_{ij})$ is used to examine the current SPM realization. The

231 convolution of the final SPM prediction should be the same as the target coarse proportion. Specifically, if the

232 convolution of the current SPM realization, $L_k(V_{ij})$, is larger than the target proportion $F_k(V_{ij})$, a positive

233 gradient is produced and the energy is reduced to decrease the neuron output (see Eq. (12) and Eq. (13)) to cope

234 with this overestimation issue. On the contrary, if $L_k(V_{ij})$ is smaller than $F_k(V_{ij})$, a negative gradient is

235 produced and the neuron output is increased correspondingly to cope with underestimation. After a number of

236 iterations (usually over 1000), $L_k(V_{ij})$ will approach $F_k(V_{ij})$, suggesting that the convolution of the final

237 prediction is almost identical to the target coarse proportion contaminated by the PSF effect. In this way, the

238 PSF effect in SPM is considered and a more reliable sub-pixel class distribution can be reproduced. It should be

239 noted that the proposed HNN-based SPM method accounting for the PSF is suitable for *any* PSF. Its

240 implementation is not affected by the specific form of PSF. Once the PSF of the sensor is available or estimated,

241 it can be used readily in the proposed method, as shown in Eq. (20).

242 As suggested in Tatem et al. (2001), for the HNN, the network will converge to similar energy minima given

243 any initialization and the network will converge to an accurate prediction in fewer iterations if a

244 proportion-constrained initialization is used. This scheme was employed in the proposed method for faster

245 convergence of the optimization. According to Eq. (6), in the estimated coarse proportions images, if a pixel is

246 presented as a pure pixel (e.g., belongs entirely to class k), all sub-pixels in the local window centered at the

247 coarse pixel must belong to class k. Thus, for any pure pixel in the coarse proportion image for class k, we

248 directly initialize the neuron outputs of all sub-pixels within it as 1 for class k and 0 for other classes. These

249 values are fixed and not changed in the optimization process. For mixed pixels, random initialization (between

250 0 and 1) was applied.

251

3. Experiments

Experiments were carried out on three groups of synthetic datasets, including a dataset with six different targets, a land cover map with multiple classes, and a multispectral image. They were used to test the performance of SPM methods on different typical shapes in Section 3.1, multiple classes in Section 3.2 and the case involving realistic unmixing in Section 3.3. As mentioned earlier, the proposed method is suitable for any PSF. The estimation of the PSF of sensors is still an open problem, and uncertainty unavoidably exists in the process. It is beyond the scope of this paper to estimate the PSF. Alternatively, to concentrate solely on the performance of SPM, all coarse data for the three groups of datasets were produced by convolving the available fine spatial resolution data, using a Gaussian PSF shown in Eq. (9), which is a widely used PSF (Campagnolo & Montano, 2014; Huang et al., 2002; Manslow & Nixon, 2002; Townshend et al., 2000; Van der Meer, 2012; Wenny et al., 2015). The width of the PSF was set to half of the coarse pixel size. Based on this strategy, the fine spatial resolution data are known perfectly and can be used as a reference for evaluation. All SPM results were evaluated both visually and quantitatively. For quantitative evaluation, the classification accuracy of each class and the overall accuracy (OA) in terms of the percentage of correctly classified pixels were used. In addition, to emphasize the improvement of the proposed method over the other methods, an index called the reduction in remaining error (RRE) (Wang et al., 2015) was also used, as calculated below

$$\text{RRE} = \frac{\text{RE}_1 - \text{RE}_0}{\text{RE}_1} \times 100\% \qquad (21)$$

where RE_1 and RE_0 are the remaining errors of OA (i.e., 100%-OA) for the benchmark method and the proposed method, respectively.

3.1. Experiment on the six targets

In this experiment, six binary images (pixel value 1 for white target while 0 for black background) with different targets were used for validation. They represent typical, basic shapes in nature. All six images have a

276   spatial size of 56 by 56 pixels and were marked as T1-T6, as shown in Fig. 1(a). Each image was degraded with

277   a Gaussian PSF and a zoom factor of 7, generating coarse images with 8 by 8 pixels, as shown in Fig. 1(b). The

278   coarse images are exactly the simulated coarse proportions of the white targets in each image.

279   Fig. 3 shows the relation between the PSF-convolved coarse proportions and actual proportions for the six

280   white targets. The actual proportions were generated by averaging the sub-pixel class indicators within each

281   coarse pixel. As observed from the plots, the proportions are very different to the actual values due to the PSF

282   effect. For example, in all six plots, many proportions should be 0 (i.e., pure background pixel and no target

283   pixel in the coarse pixel), but were actually calculated as values larger than 0 (i.e., mixed pixel). The reason is

284   that although no target pixels exist in a coarse pixel, they may be located in neighboring pixels. According to

285   Eq. (6), these neighboring pixels will contaminate the center pixel which will then not be recognized as a pure

286   background pixel. The accuracies of the coarse proportions were quantified in terms of root mean square error

287   (RMSE) and correlation coefficient (CC), as listed in Table 1. The uncertainty in the PSF-convolved coarse

288   proportions motivates the development of SPM methods considering the PSF effect.

289

290   Table 1 Accuracy of the coarse proportion images for the six targets

	T1	T2	T3	T4	T5	T6
RMSE	0.0421	0.0602	0.0671	0.0707	0.0924	0.0972
CC	0.9949	0.9902	0.9820	0.9868	0.9677	0.9668

291

292   The SPM results of the HNN without PSF (that is, with ideal PSF) and with the Gaussian PSF are shown in

293   Fig. 2(c) and Fig. 2(d), respectively. It is seen clearly that by considering the PSF effect, more accurate SPM

294   results can be produced. In the results for target T1-T3, the proposed method produces more compact shapes

295   that are closer to the reference. For T4 and T5, the proposed method produces a straighter line than the HNN

296   without PSF. In T6, the more complex boundaries of the target are reproduced by the proposed method.
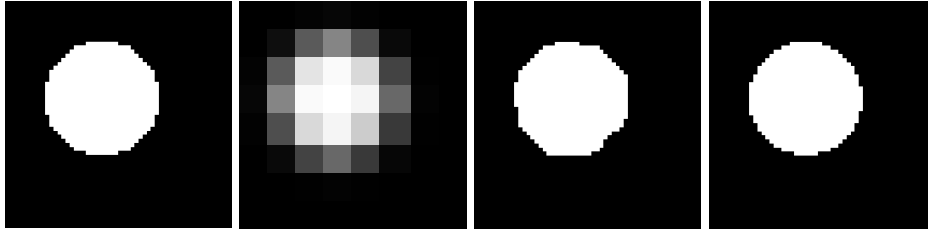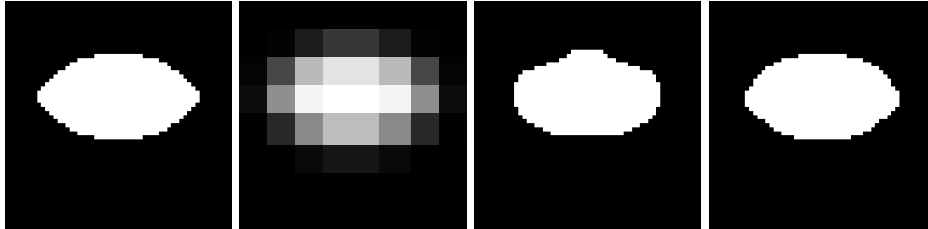
297

298

299
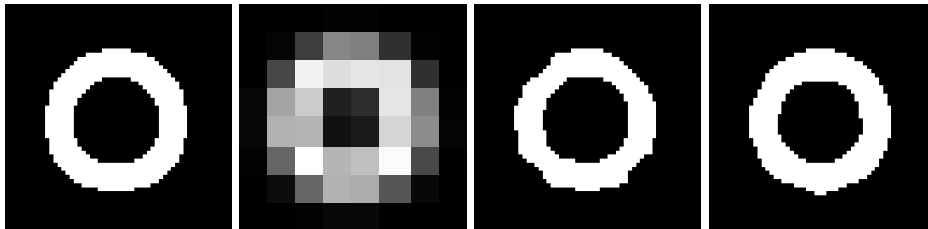
300   (a)   (b)   (c)   (d)
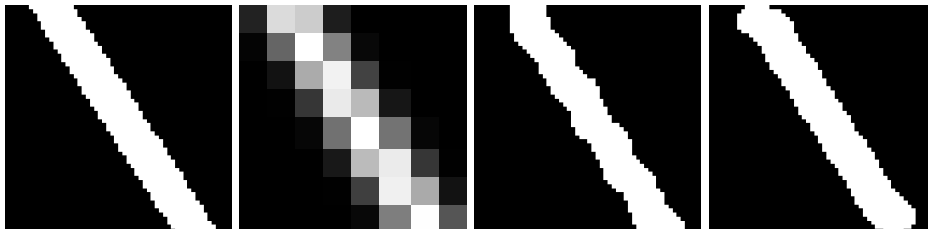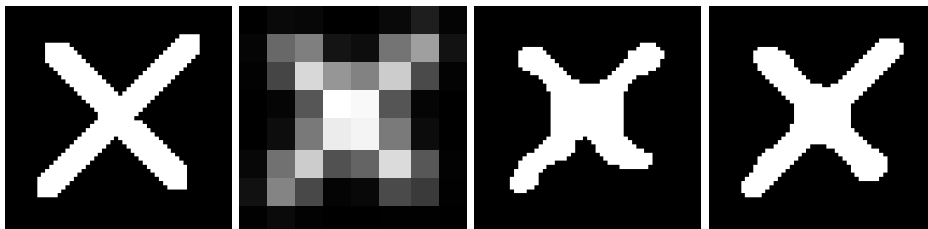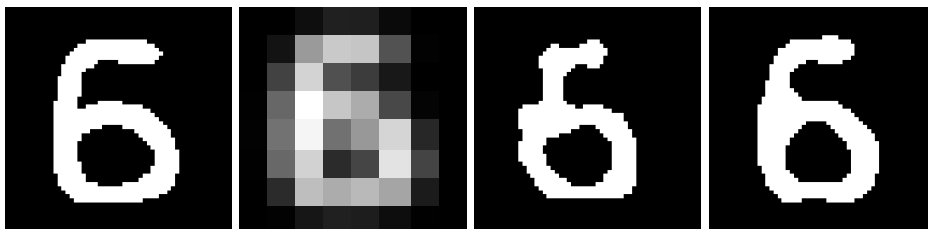
301

302

303

304

305

306

307   Fig. 2 SPM results of six targets. (a) Reference images (56 by 56 pixels). (b) Coarse images (8 by 8 pixels) produced by degrading (a)

308   with a Gaussian PSF and a factor of 7. (c) SPM results produced using the HNN without PSF (or with ideal PSF). (d) SPM results

309   produced using the proposed HNN with the Gaussian PSF. Lines 1-6 are results for T1-T6.
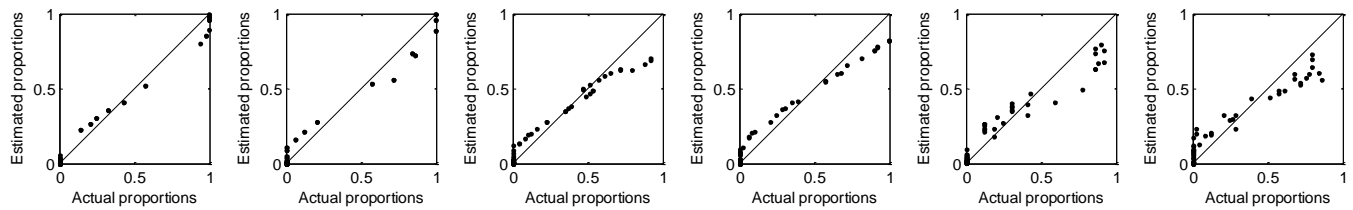
310

Fig. 3 Relation between the actual proportions (for white target) and proportions (for white target) contaminated due to the PSF effect for the six binary images (z=7). From left to right are results for T1-T6.

Quantitative assessment in terms of OA (accuracy statistics for both target and background in each image) is listed in Table 2. As mentioned earlier, for pure pixels, all sub-pixels within them are simply assigned to the same class to which the pure pixel belongs. As suggested by the existing literature (Mertens et al., 2003), this copy process will only increase the SPM accuracy statistics without providing any useful information on the actual performance of the SPM methods. Hence, for the synthetic coarse images, we did not consider the pure pixels in the accuracy statistics. The quantitative evaluation was conducted for two different zoom factors, z=4 and 7. As observed from the table, the HNN with PSF produces a larger OA than the HNN without PSF. Moreover, the advantage tends to be more obvious when a larger zoom factor is involved. More precisely, for T2 and T5, using the proposed method, the accuracy gains are below 1% for z=4, but increase to be above 2% for z=7. For T6, the proposed method considering the PSF increases the OA by 1.4% for z=4 and 4.7% for z=7. In addition, all RREs are generally large (over 10%) and some even reach over 60%, suggesting that the accuracy increase is obvious.

Table 2 OA (%) of HNN-based SPM with two different schemes for the six binary images

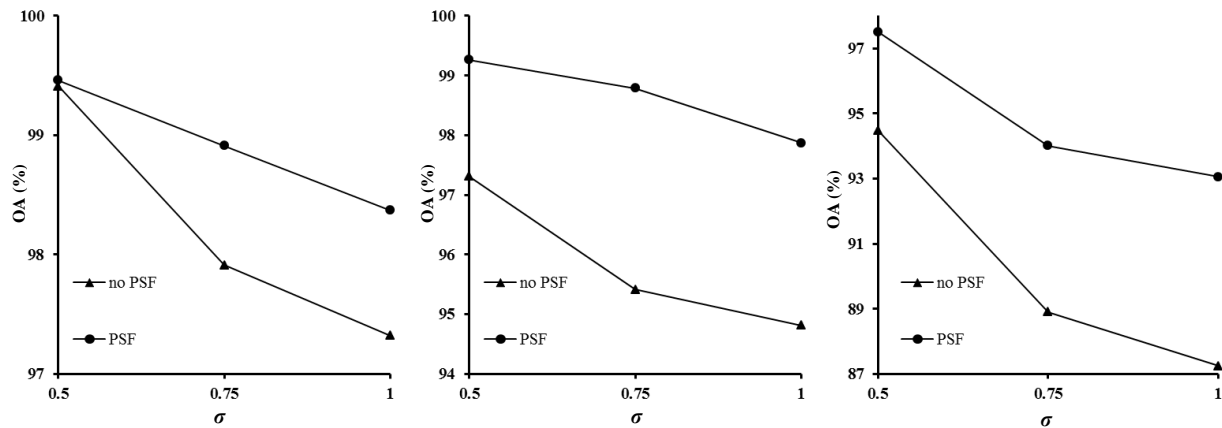|		T1	T2	T3	T4	T5	T6
z=4	no PSF	99.34	98.72	98.00	98.44	98.30	96.66
	PSF	99.34	99.52	99.26	99.19	98.67	98.08
	RRE	0%	62.50%	63.00%	48.08%	21.76%	42.51%
z=7	no PSF	99.41	97.31	97.89	97.34	94.48	90.53
	PSF	99.46	99.26	98.16	97.91	97.51	95.18
	RRE	8.47%	72.49%	12.80%	21.43%	54.89%	49.10%

Fig. 4 The accuracy of the two SPM methods in relation to the width of the PSF (in units of coarse pixel, which was produced by

degrading Fig. 2(a) with a factor of 7). From left to right are results for T1, T2 and T5, respectively.

The influence of the width of the Gaussian PSF was also analyzed, as shown in Fig. 4. The fine spatial

resolution T1, T2 and T5 images were degraded with a factor of 7. Three PSF sizes, 0.5, 0.75 and 1 coarse

pixels, were considered for each target. Three observations can be made from the results in Fig. 4. First, for all

PSF sizes, the consideration of the PSF effect can lead to consistently larger OA than that produced without the

PSF. Second, the accuracy of SPM methods decreases as the width of the PSF increases, no matter whether the

PSF is accounted for or not. This is because more neighboring sub-pixels are involved in the convolution

process and the SPM problem becomes more complex as the width increases. Third, as the width increases, the

advantage of considering the PSF is more obvious.

3.2. Experiment on the land cover map with multiple classes

A land cover map produced from an aerial photograph covering an area in Bath, UK was used in this

experiment, as shown in Fig. 5. The image has a spatial resolution of 0.6 m, and a spatial size of 360 by 360

pixels. Four classes were identified in the land cover map, including roads, trees, buildings and grass. The map

was degraded with a factor of 8 and a Gaussian PSF, generating four proportion images at a spatial resolution

of 4.8 m. The relation between the simulated coarse proportions and actual proportions is shown in the plots in

Fig. 6. Table 3 lists the accuracies of the proportions. Similarly to the observation in Fig. 3 and Table 1, the two

types of proportions are very different due to the PSF effect.
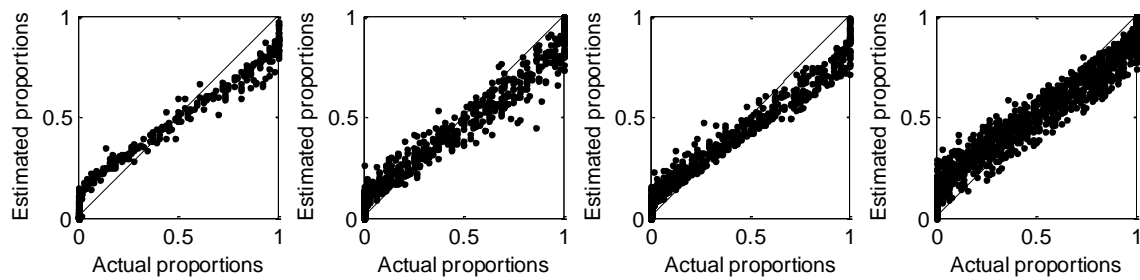
Roads ▇ Trees ▇ Buildings ▇ Grass

352

353

354

355 Fig. 5 The land cover map. (a) Original aerial photograph. (b) Reference map drawn manually from (a).

356

357

358 Fig. 6 Relation between the actual proportions and proportions contaminated due to the PSF effect for the land cover map (z=8). From

359 left to right are results for roads, trees, buildings and grass.

360

361   Table 3 Accuracy of the coarse proportion images for the land cover map

	Roads	Trees	Buildings	Grass	Mean
RMSE	0.0440	0.0576	0.0591	0.0924	0.0633
CC	0.9866	0.9867	0.9844	0.9792	0.9842

362

363   The proposed method is not only compared to the original HNN method, but also to several typical SPM

364 methods. As mentioned in the Introduction, there are mainly two families of SPM methods for post-processing

365 of spectral unmixing. One is the method considering the relation between sub-pixels and neighboring pixels,

366 while the other considers the relation between sub-pixels. The SPSAM (Mertens et al., 2006) and RBF (Wang

367 et al., 2014a) methods were selected for the former and PSA (Makido et al., 2007) was selected for the latter.

368   For these three benchmark methods, the number of sub-pixels for each class needs to be determined first. The

369   numbers were calculated according to Eq. (10), where uncertainty from the PSF effect exists in the coarse

370   proportions. The SPM results of all five methods are presented in Fig. 7.
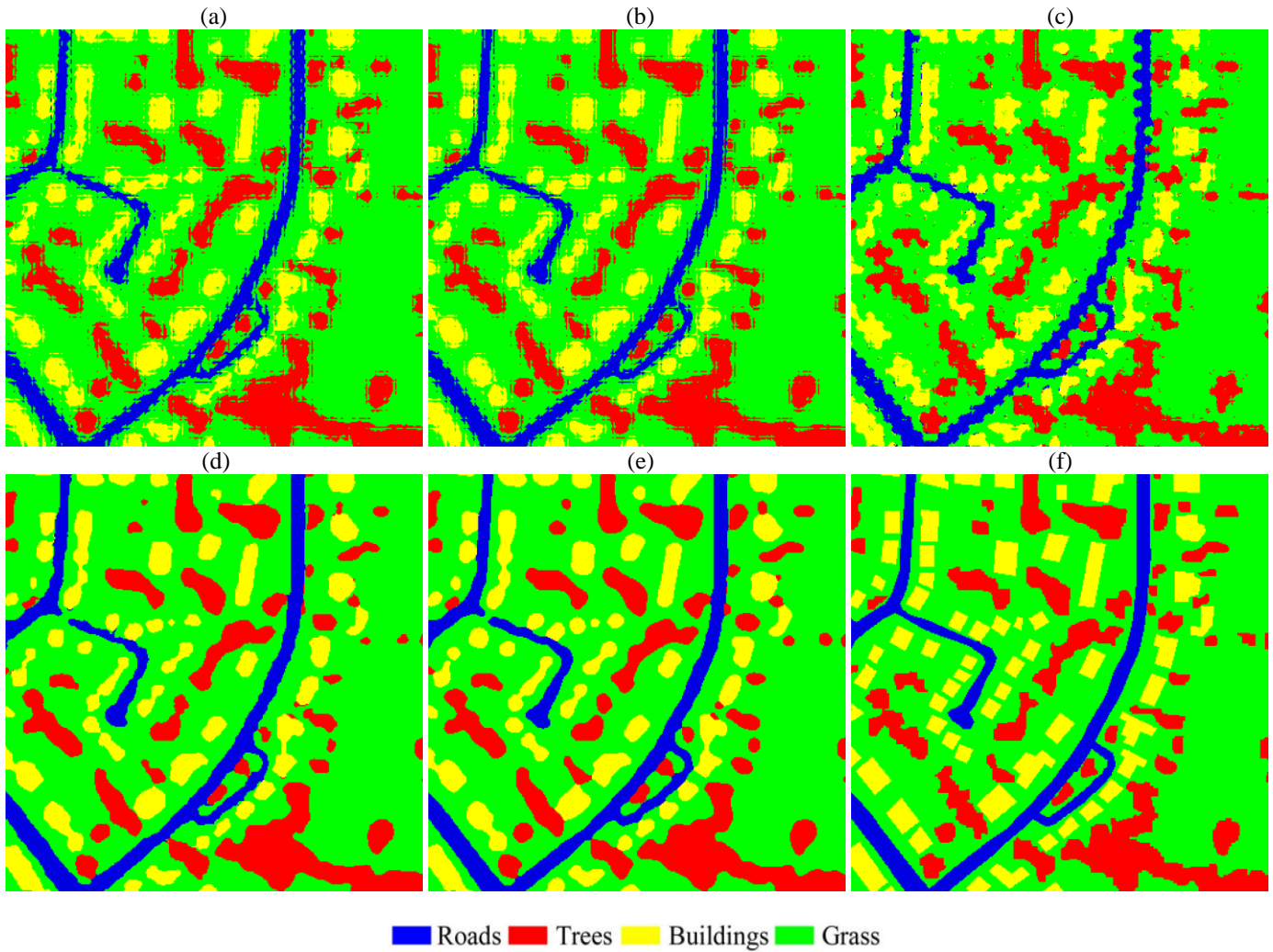
371

372

Fig. 7 SPM results of the land cover map with 360 by 360 pixels (z=8). (a) SPSAM (no PSF). (b) RBF (no PSF). (c) PSA (no PSF). (d) HNN (no PSF). (e) The proposed HNN with PSF. (f) Reference.

379

380   Due to the uncertainty in the coarse proportions, the SPM predictions of SPSAM and RBF contain a number

381   of jagged artifacts and the boundaries of classes are rough. Although PSA is able to enhance the performance

382   and produce a more compact result, the class boundaries are still not smooth and some noisy pixels exist.

383   Different from the three methods, the original HNN method produces a cleaner result and the class boundaries

384 are smoother, although the PSF is not considered. The reason is that the HNN is not absolutely slavish to the

385 coarse proportions, and can remove isolated pixels and produce a compact result by the two spatial clustering

386 functions $G1$ and $G2$ (see Eq. (16) and Eq. (17)). However, there are some needle-like artifacts for restoration

387 of roads and trees in the HNN result. Using the proposed method accounting for the PSF effect, the result is

388 more accurate than the original HNN without the PSF method. For example, the prediction of the roads by the

389 proposed method is smoother, and needle-like artifacts are removed. The result of the proposed method is the

390 closest to the reference in Fig. 7(f) amongst all five methods.

391

392 Table 4 SPM accuracy (%) of the different SPM schemes for the experiment on the land cover map

		SPSAM (no PSF)	RBF (no PSF)	PSA (no PSF)	HNN (no PSF)	HNN (PSF)
z=4	Roads	94.59	94.64	93.81	98.92	99.78
	Trees	92.16	92.53	91.45	94.38	95.41
	Buildings	91.20	91.69	90.43	93.50	95.28
	Grass	93.82	94.10	93.22	97.86	98.57
	OA	93.17	93.47	92.50	96.62	97.58
	RRE (in OA)	64.57%	62.94%	67.73%	28.40%	
z=8	Roads	88.24	88.86	87.26	95.13	98.03
	Trees	86.20	87.48	86.13	85.20	90.08
	Buildings	82.51	83.81	81.83	82.92	88.64
	Grass	91.77	90.98	91.74	95.97	95.85
	OA	89.42	89.15	89.23	92.15	94.00
	RRE (in OA)	43.29%	44.70%	44.29%	23.57%	

393

394 Table 4 is the accuracy for the five SPM methods, where two zoom factors, 4 and 8, were tested. Again, the

395 pure pixels were not considered in the accuracy statistics. For both zoom factors, the proposed HNN with PSF

396 method produces the greatest accuracy for all classes, and thus, the largest OA amongst all methods. More

397 specifically, SPSAM, RBF and PSA have very similar accuracies. The three methods produce OA of around 93%

398 for z=4 and 89% for z=8. Compared to the three benchmark methods, the HNN without PSF method is more

399 accurate. For z=4 and 8, the OA is increased by around 3.5% and 3%, respectively. With respect to the

400 proposed HNN with PSF method, the accuracies of roads, trees, buildings and grass are increased by at least

401   5%, 3%, 3.5% and 4% in comparison with SPSAM, RBF and PSA for z=4, and correspondingly, the OA is

402   increased by over 4%. In addition, with the PSF, the OA is 1% larger than the original HNN method. For z=8,

403   the accuracies of roads, trees and buildings for the proposed method are 3%, 5% and 6% larger than for the

404   HNN without PSF method. Moreover, the OA of the proposed method is 4.6%, 4.9%, 4.8% and 1.9% larger

405   than the SPSAM, RBF, PSA and HNN without PSF methods, and the corresponding RREs are 43.29%,

406   44.70%, 44.29% and 23.57%.

407

408   *3.3. Experiment on the multispectral image*

409   In this experiment, to control the experimental analysis and ensure the perfect reliability of the reference, a

410   synthesized multispectral image was used. The original multispectral image was acquired by the Landsat-7

411   Enhanced Thematic Mapper sensor in August 2001 and covers a farmland in the Liaoning Province, China.

412   The spatial resolution is 30 m. The studied area has a spatial size of 240 by 240 pixels and covers mainly four

413   land cover classes (marked as C1-C4). Fig. 8(a) and Fig. 8(b) show the original multispectral image and the

414   corresponding manually digitized reference map. From the reference map, the mean and variance of each land

415   cover class in the original 30 m Landsat image (bands 1-5 and 7 were considered) were calculated. Referring to

416   Fig. 8(b), the six-band 30 m resolution multispectral image was synthesized based on the random normal

417   distribution and the mean and variance of the classes. Fig. 8(c) shows the synthesized multispectral image. A

418   240 m coarse image, a spatial resolution comparable to that of medium-spatial-resolution systems such as

419   Moderate Resolution Imaging Spectroradiometer (MODIS), was created by degrading the synthesized 30 m

420   image with a factor of 8, using a Gaussian PSF. Fig. 8(d) shows the 240 m image. With this strategy, the

421   reference land cover map at 30 m is known perfectly for accuracy assessment.

422   Spectral unmixing was first performed on the 240 m coarse image using the classical linear spectral mixture

423   model. Fig. 9 is the relation between the estimated proportions and actual proportions for the four classes. The

424   errors are visually larger than those in Fig. 6. This is because the errors in proportions in this experiment

425   originate not only from the PSF effect, but also from the spectral unmixing process. This can be supported by

the results in Table 5, where the accuracies of the proportions were evaluated using two different references. The convolved proportions were produced by convolving the 30 m land cover map in Fig. 8(b) with the Gaussian PSF. Using the convolved proportions as reference, errors can be observed from only spectral unmixing. As shown in the table, the spectral unmixing errors are particularly large for C1 and C2 (with RMSEs of 0.0418 and 0.0303, respectively). Furthermore, as the PSF introduces additional uncertainty, the accuracies evaluated using the actual proportions as reference are smaller than those for the convolved proportions.
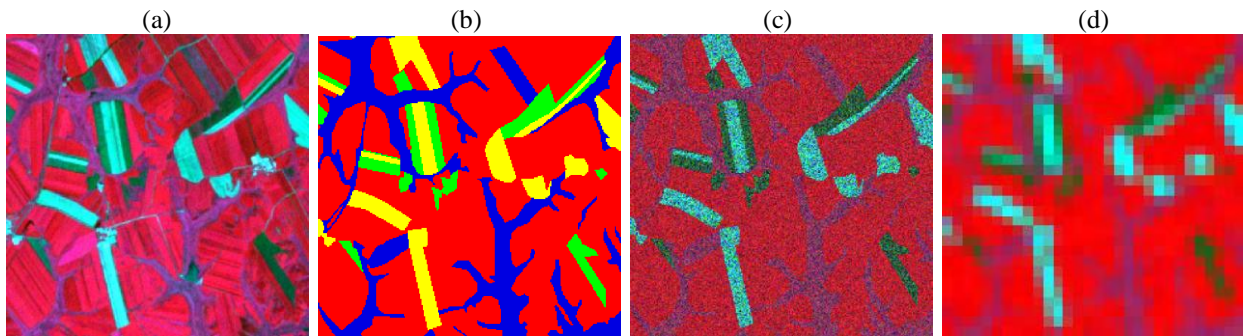

Fig. 8 The multispectral image used for experiment 3. (a) Original 30 m multispectral image (bands 432 as RGB). (b) Reference map drawn manually from (a). (c) Synthesized 30 m multispectral image (bands 432 as RGB). (d) 240 m coarse image produced by degrading (c) with a factor of 8 using a Gaussian PSF.
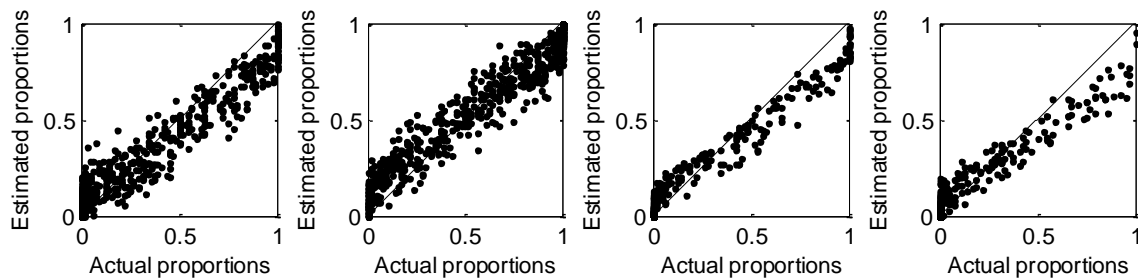

Fig. 9 Relation between the actual proportions and proportions estimated from spectral unmixing for the multispectral image (z=8). From left to right are results for C1-C4.

Based on the estimated proportions, SPM was implemented and the results of the five methods are shown in Fig. 10. Failing to account for the PSF, the SPSAM, RBF and PSA predictions are dominated by noisy pixels

446 and spurs on boundaries between classes. As the original HNN method is not completely slavish to the coarse

447 proportions, it can remove the noisy pixels and spurs and produce a smoother result than the SPSAM, RBF and

448 PSA. In Fig. 10(d), however, there are jagged boundaries, such as for C3 and C4. The prediction is further

449 enhanced by considering the PSF effect in the proposed method. The quantitative assessment in Table 6

450 suggests that the proposed method produces a larger accuracy for all four classes as well as a larger OA than the

451 other four SPM methods. Note that in this experiment, all pixels were considered in accuracy statistics,

452 including pure pixels. This is because whether a pixel is pure or not is determined by spectral unmixing and we

453 are concerned about the performance of spectral unmixing. The OA of the proposed method is 91.86%, with a

454 gain of more than 5% over SPSAM, RBF and PSA. Compared with the HNN without PSF, the proposed

455 method increases the accuracies of C1 and C4 by 4.5% and 5.5% and the OA by 1.3%. All RREs (in OA) are

456 large, which means that the proposed method reduces the errors obviously. Note that due to the uncertainty in

457 spectral unmixing, the OA of the proposed method is smaller than that for the land cover map in Table 2 ($z=8$).

458

459 Table 5 Accuracy of the coarse proportion images for the multispectral image

		C1	C2	C3	C4	Mean
Actual proportion	RMSE	0.0873	0.0950	0.0517	0.0529	0.0717
	CC	0.9703	0.9766	0.9844	0.9692	0.9751
Convolved proportion	RMSE	0.0418	0.0303	0.0085	0.0206	0.0253
	CC	0.9885	0.9957	0.9992	0.9913	0.9937

460

461

(a)   (b)   (c)

462
463
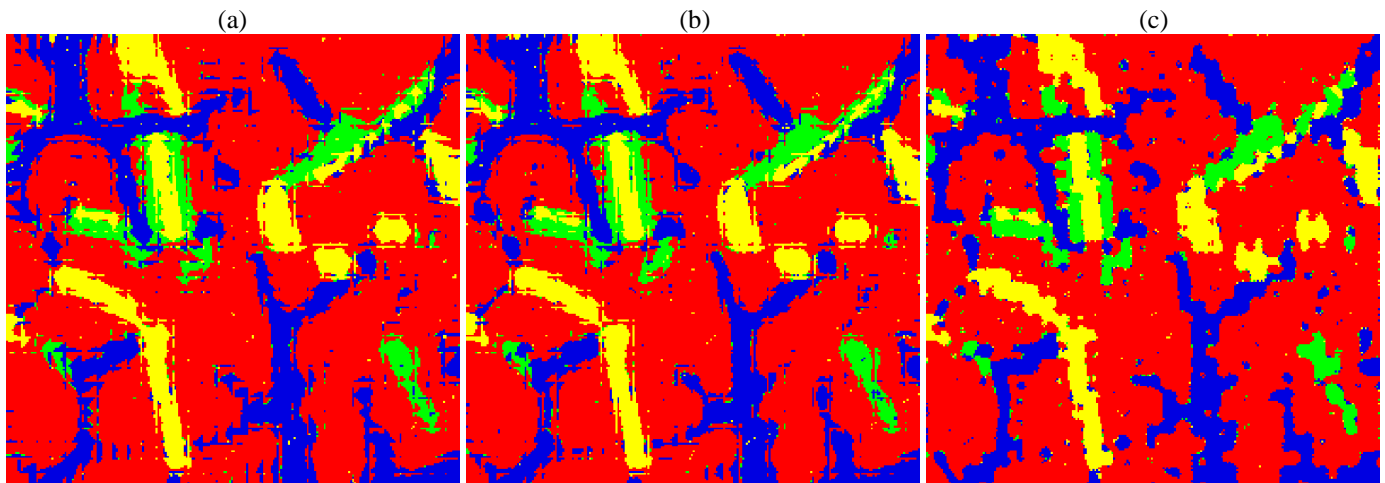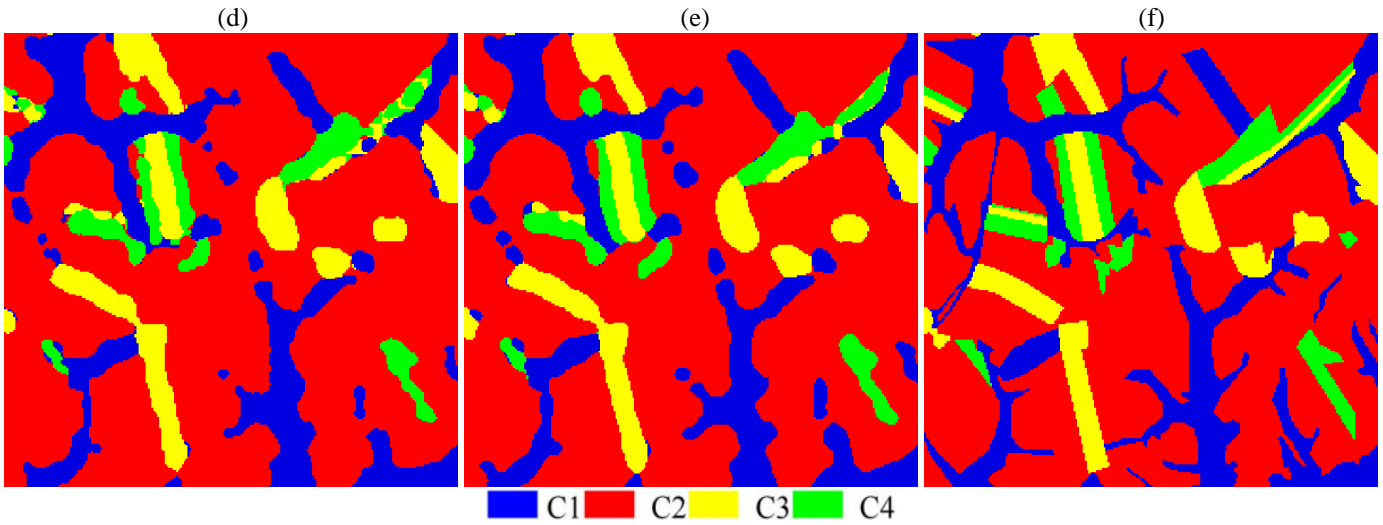
Fig. 10 SPM results of the multispectral image with 240 by 240 pixels (z=8). (a) SPSAM (no PSF). (b) RBF (no PSF). (c) PSA (no PSF). (d) HNN (no PSF). (e) The proposed HNN with PSF. (f) Reference.

Table 6 SPM accuracy (%) of the different SPM schemes for the experiment on the multispectral image

	SPSAM (no PSF)	RBF (no PSF)	PSA (no PSF)	HNN (no PSF)	HNN (PSF)
C1	75.88	77.65	75.98	76.89	81.40
C2	90.92	91.71	90.92	96.57	96.26
C3	82.50	84.30	81.68	87.08	89.81
C4	71.18	73.38	72.95	77.75	83.15
OA	85.91	87.07	85.95	90.57	91.86
RRE (in OA)	42.23%	37.05%	42.06%	13.68%	

4. Discussion

The PSF effect exists ubiquitously in remote sensing images and the pixel signal is contaminated by its neighbors as a result. Existing SPM methods are generally performed based on the assumption of the ideal square wave filter-based PSF and treat the signal of a coarse pixel as the mean of sub-pixel signals within it. This assumption ignores the effect from neighbors and limits unnecessarily the accuracy of SPM predictions. As shown in the experimental results, the SPSAM, RBF and PSA predictions contain noticeable errors where the PSF is ignored. Note that the performances of the SPSAM, RBF and PSA methods are not as satisfactory as

481 demonstrated in the literature where they were proposed (Makido et al., 2007; Mertens et al., 2006; Wang et al.,

482 2014a). The reason is that in the experimental design in the literature, the coarse images were simulated using

483 the ideal square PSF and, thus, the sub-pixel maps can be satisfactorily reproduced by ignoring the PSF effect.

484 The proposed SPM approach that considers the PSF effect is developed based on the iterative HNN method.

485 The computing time is the product of the average time consumed in each iteration and the number of required

486 iterations. When considering the PSF effect, more sub-pixels are involved in the convolution process (see Eq.

487 (20)) and more time is needed in each iteration. Moreover, the convergence rate is slower and a larger number

488 of iterations is required. Thus, the proposed method has larger computational cost than the original HNN

489 method without the PSF. In the experiments, the original HNN method is able to converge after 1000 iterations,

490 but the proposed method needs 3000 iterations instead. For SPM of the multispectral image, the running time

491 of the original HNN and the proposed method is 1 and 5 hours, respectively. Note that the computational cost

492 of a SPM method is positively related to the spatial size of the input coarse image, number of classes and zoom

493 factor.

494 This paper considers using HNN to cope with the PSF effect. The solution is identified as modifying the

495 proportion constraint term in the original HNN using a convolution process where contributions from

496 neighboring coarse pixels are accounted for. It would be worthwhile to develop other solutions based on

497 existing SPM methods, such as PSA and the STHSPM methods. For example, in the original PSA method,

498 pixel swapping is allowed only within a coarse pixel. To account for the PSF, the SPM method can be extended

499 by allowing sub-pixel swaps not only within a coarse pixel, but also between coarse pixels. The number of

500 allowable sub-pixel swap between coarse pixels would be a key issue that needs to be addressed. Moreover, it

501 would also be interesting to consider developing artificial intelligence-based methods (e.g., genetic algorithm

502 and PSO, etc.). In such methods, the solutions in the set (called population in genetic algorithm and swarm in

503 PSO) can be updated iteratively according to the fitness values (calculated according to the pre-defined

504 objective) by using related operators (such as crossover and mutation in genetic algorithm and position update

505 in PSO). An optimal solution is expected to be produced after a number of generations. A critical issue for this

type of approach would be the definition of the objective, where a constraint term is needed for taking the PSF effect into consideration. Both the prediction accuracy and computational cost will be important indices to identifying an effective method.

Each sensor has its own PSF size. Based on the assumption of a Gaussian filter, some studies were conducted to estimate the PSF size of satellite sensor images. Radoux et al. (2016) estimated the PSF size of Landsat 8 and Sentinel-2 images. It was found that the full-width at half-maximum (FWHM) for Landsat 8 red band is 1.70 pixels (amounting to a width of 0.72 pixel) and ranges from 1.67 to 2.21 pixels (i.e., a width from 0.71 to 0.94 pixel) for Sentinel-2 bands. Campagnolo & Montano (2014) estimated the PSF size of MODIS images at different view zenith angles. The size of the PSF is a critical factor affecting the performance of the proposed method, as displayed in Fig. 4. As the size increases, more neighboring sub-pixels contaminate the center coarse pixel, and the accuracy of the proposed method will decrease correspondingly. However, the advantage of the proposed method over the traditional method (i.e., accuracy gain) is obvious across different PSF sizes, especially for large ones. The encouraging performance will promote the application of the proposed method for sensors with various PSF sizes.

The main objective of this paper was to find a generic solution to address the PSF effect in SPM and increase the accuracy of SPM predictions. A Gaussian PSF was assumed for convenience in the experimental validation. In reality, the PSF may not be the Gaussian filter, especially for sensors with a rotating/scanning mirror which will ensure that the shape has a directional component. For example, the MODIS sensor PSF was claimed to be triangular in the along-scan direction but rectangular in the along-track direction in Tan et al. (2006). As seen from Eq. (20), however, the proposed method is suitable for any PSF. Thus, in real cases, if the PSF is known or estimated reliably, it can be used readily in the proposed method. This paper provides a first guidance to increase SPM accuracy by considering the PSF effect. It could also help to initiate research on PSF estimation that would ultimately provide the information needed for the use of the proposed method. The PSF estimation mainly includes determination of the specific form of the function and related parameters. This is part of our ongoing research.

531   The spatial clustering functions $G1$ and $G2$ in the HNN make the proposed method more appropriate for

532   SPM in the H-resolution case, where the objects of interest are larger than the pixel size of the input coarse

533   image (Atkinson, 2009). In the L-resolution case where the objects of interest are smaller than the pixel size,

534   alternative prior spatial structure information-based models, such as the semivariogram-based model in Tatem

535   et al. (2002), are more suitable, and should be applied. It would also be worthy of developing models that can

536   adaptively cope with different spatial patterns. Ge et al. (2016) performed a pioneering study for this issue.

537   Although the proposed method can increase the SPM accuracy, uncertainty still exists. Based on Eq. (6), the

538   ideal SPM solution is identified as the one that when convolved with the PSF, predicts the coarse proportion.

539   There can be multiple solutions satisfying this condition, leading to the perfect coherence constraint. The

540   uncertainty related to this issue can be further reduced by using additional information, such as sub-pixel

541   shifted remote sensing images (Ling et al., 2010; Zhong et al., 2014), panchromatic images (Ardila et al., 2011;

542   Li et al., 2014; Nguyen et al., 2011), high resolution color images (Mahmood et al., 2013), digital elevation

543   models (Huang et al., 2014), time-series images (Wang et al., 2016), segmentation data (Aplin & Atkinson,

544   2001; Robin et al., 2008) or shape information (Ling et al., 2012). It would be an interesting challenge to design

545   the appropriate model to incorporate such additional information into the proposed method considering the

546   PSF effect for possible enhancement in future research.

547

548

549   **5. Conclusion**

550

551   This paper presents a HNN-based method to account for the PSF effect in SPM and increase the SPM

552   predictions. Based on the recognition of the PSF as a real effect, the coarse proportions are viewed as the

553   convolution of sub-pixels within the local window centered at the coarse pixel, rather than of only the

554   sub-pixels within the coarse pixel. In the proposed HNN-based method, the interim SPM realization is

555   convolved with the PSF and compared with coarse proportions for further updating. The final solution is

identified as the one that when convolved with the PSF, is the same as the input coarse proportion. The proposed method is a generic method suitable for any PSF. The effectiveness of the proposed method was validated using three groups of datasets.

Acknowledgment

References

Aplin, P., & Atkinson, P. M. (2001). Sub-pixel land cover mapping for per-field classification. *International Journal of Remote Sensing*, 22, 2853–2858.

Ardila, J. P., Tolpekin, V. A., Bijker, W., Stein, A. (2011). Markov-random-field-based super-resolution mapping for identification of urban trees in VHR images. *ISPRS Journal of Photogrammetry and Remote Sensing*, 66, 762–775.

Atkinson, P. M. (1997). Mapping sub-pixel boundaries from remotely sensed images. *Innov. GIS 4*, 166–180.

Atkinson, P. M. (2005). Sub-pixel target mapping from soft-classified, remotely sensed imagery. *Photogrammetric Engineering and Remote Sensing*, 71, 839–846.

Atkinson, P. M. (2008). Super-resolution mapping using the two-point histogram and multi-source imagery. *GeoENV VI: Geostatistics for Environmental Applications*, 307–321.

Atkinson, P. M. (2009). Issues of uncertainty in super-resolution mapping and their implications for the design of an inter-comparison study. *International Journal of Remote Sensing*, 30, 5293–5308.

Bioucas-Dias, J. M., Plaza, A., Dobigeon, N., Parente, M., Du, Q., Gader, P., Chanussot, J. (2012). Hyperspectral unmixing overview: Geometrical, statistical and sparse regression-based approaches. *IEEE Journal of Selected Topics in Applied Earth Observations and Remote Sensing*, 5, 354-379.

583 Boucher, A., & Kyriakidis, P. C. (2006). Super-resolution land cover mapping with indicator geostatistics. *Remote Sensing of*
584   *Environment*, 104, 264–282.

585 Campagnolo, M. L., & Montano, E. L. (2014). Estimation of effective resolution for daily MODIS gridded surface reflectance
586   products. *IEEE Transactions on Geoscience and Remote Sensing*, 52, 5622–5632.

587 Chen, Y., Ge, Y., Heuvelink, G. B. M., Hu, J., Jiang, Y. (2015). Hybrid constraints of pure and mixed pixels for soft-then-hard
588   super-resolution mapping with multiple shifted images. *IEEE Journal of Selected Topics in Applied Earth Observations and*
589   *Remote Sensing*, 8, 2040–2052.

590 Foody G. M., & Doan, H. T. X. (2007). Variability in soft classification prediction and its implications for sub-pixel scale change
591   detection and super-resolution mapping. *Photogrammetric Engineering and Remote Sensing*, 73, 923-933.

592 Ge, Y., Chen, Y., Li, S., Jiang, Y. (2014). Vectorial boundary-based sub-pixel mapping method for remote-sensing imagery.
593   *International Journal of Remote Sensing*, 35, 1756–1768.

594 Ge, Y., Chen, Y., Stein, A., Li, S., Hu, J. (2016). Enhanced subpixel mapping with spatial distribution patterns of geographical
595   objects. *IEEE Transactions on Geoscience and Remote Sensing*, 54, 2356–2370.

596 Gu, Y., Zhang, Y., Zhang, J. (2008). Integration of spatial-spectral information for resolution enhancement in hyperspectral images.
597   *IEEE Transactions on Geoscience and Remote Sensing*, 46, 1347–1358.

598 Heinz, D. C., & Chang, C. I. (2001). Fully constrained least squares linear spectral mixture analysis method for material
599   quantification in hyperspectral imagery. *IEEE Transactions on Geoscience and Remote Sensing*, 39, 529–545.

600 Kasetkasem, T., Arora, M. K., Varshney, P. K. (2005). Super-resolution land-cover mapping using a Markov random field based
601   approach. *Remote Sensing of Environment*, 96, 302–314.

602 Keshava N., & Mustard, J. F. (2002). Spectral unmixing. *IEEE Signal Processing Magazine*, 19, 44–57.

603 Huang, C., Townshend, R.G., Liang, S., Kalluri, S. N. V., DeFries, R. S. (2002). Impact of sensor's point spread function on land
604   cover characterization: assessment and deconvolution. *Remote Sensing of Environment*, 80, 203–212.

605 Huang, C., Chen, Y., Wu, J. (2014). DEM-based modification of pixel-swapping algorithm for enhancing floodplain inundation
606   mapping. *International Journal of Remote Sensing*, 35, 365–381.

607 Li, L., Chen, Y., Xu, T., Liu, R., Shi, K., Huang, C. (2015). Super-resolution mapping of wetland inundation from remote sensing
608   imagery based on integration of back-propagation neural network and genetic algorithm. *Remote Sensing of Environment*, 164,
609   142–154.

610 Li, X., Ling, F., Du, Y., Zhang, Y. (2014). Spatially adaptive superresolution land cover mapping with multispectral and
611   panchromatic images. *IEEE Transactions on Geoscience and Remote Sensing*, 52, 2810-2823.

Lin, H., Bo, Y., Wang, J., Jia, X. (2011). Landscape structure based super-resolution mapping from remotely sensed imagery. *Proceedings of International Geoscience and Remote Sensing Symposium*, 79–82.

Ling, F., Du, Y., Xiao, F., Xue, H., Wu, S. (2010). Super-resolution land-cover mapping using multiple sub-pixel shifted remotely sensed images. *International Journal of Remote Sensing*, 31, 5023–5040.

Ling, F., Li, X., Xiao, F., Fang, S., Du, Y. (2012). Object-based sub-pixel mapping of buildings incorporating the prior shape information from remotely sensed imagery. *International Journal of Applied Earth Observation and Geoinformation*, 18, 283–292.

Ling, F., Li, X., Xiao, F., Du, Y. (2014). Superresolution land cover mapping using spatial regularization. *IEEE Transactions on Geoscience and Remote Sensing*, 52, 4424–4439.

Mahmood, Z., Akhter, M. A., Thoonen, G., Scheunders, P. (2013). Contextual subpixel mapping of hyperspectral images making use of a high resolution color image. *IEEE Journal of Selected Topics in Applied Earth Observations and Remote Sensing*, 6, 779–791.

Manslow J. F., & Nixon, M. S. (2002). On the ambiguity induced by a remote sensor's PSF. In *Uncertainty in Remote Sensing and GIS*, 37–57.

Makido, Y., & Shortridge, A. (2007). Weighting function alternatives for a subpixel allocation model. *Photogrammetric Engineering and Remote Sensing*, 73, 1233-1240.

Makido, Y., Shortridge, A., Messina, J. P. (2007). Assessing alternatives for modeling the spatial distribution of multiple land-cover classes at sub-pixel scales. *Photogrammetric Engineering and Remote Sensing*, 73, 935–943.

Mertens, K. C., Verbeke, L. P. C., Ducheyne, E. I., Wulf, R. De (2003). Using genetic algorithms in sub-pixel mapping. *International Journal of Remote Sensing*, 24, 4241–4247.

Mertens, K. C., Basets, B. D., Verbeke, L. P. C., Wulf, R. De (2006). A sub-pixel mapping algorithm based on sub-pixel/pixel spatial attraction models. *International Journal of Remote Sensing*, 27, 3293–3310.

Muad A. M., & Foody, G. M. (2012). Impact of land cover patch size on the accuracy of patch area representation in HNN-based super resolution mapping. *IEEE Journal of selected topics in applied earth observation and remote sensing*, DOI: 10.1109/JSTARS.2012.2191145.

Nguyen, M. Q., Atkinson, P. M., Lewis, H. G. (2011). Super-resolution mapping using Hopfield neural network with panchromatic imagery. *International Journal of Remote Sensing*, 32, 6149–6176.

Radoux, J., Chome, G., Jacques, D. C., Waldner, F., Bellemans, N., Matton, N., Lamarche, C., Andrimont, R., Defourny, P. (2016). Sentinel-2's potential for sub-pixel landscape feature detection. *Remote Sensing*, 8, 488.

Robin, A., Hegarat-Mascle, S. Le, Moisan, L. (2008). Unsupervised subpixelic classification using coarse-resolution time series and structural information. *IEEE Transactions on Geoscience and Remote Sensing*, 46, 1359–1374.

Schowengerdt, R. A. (1997). *Remote sensing: models and methods for image processing*. San Diego: Academic Press.

Shen, Z., Qi, J., Wang, K. (2009). Modification of pixel-swapping algorithm with initialization from a sub-pixel/pixel spatial attraction model. *Photogrammetric Engineering and Remote Sensing*, 75, 557–567.

Su, Y. F., Foody, G. M., Muad, A. M., Cheng, K. S. (2012). Combining pixel swapping and contouring methods to enhance super-resolution mapping. *IEEE Journal of Selected Topics in Applied Earth Observations and Remote Sensing*, 5, 1428–1437.

Tan, B., Woodcock, C. E., Hu, J., Zhang, P., Ozdogan, M., Huang, D., Yang, W., Knyazikhin, Y., Myneni, R. B. (2006). The impact of gridding artifacts on the local spatial properties of MODIS data: Implications for validation, compositing, and band-to-band registration across resolutions. *Remote Sensing of Environment*, 105, 98–114.

Tatem, A. J., Lewis, H. G., Atkinson, P. M., Nixon, M. S. (2001). Super-resolution target identification from remotely sensed images using a Hopfield neural network. *IEEE Transactions on Geoscience and Remote Sensing*, 39, 781–796.

Tatem, A. J., Lewis, H. G., Atkinson, P. M., Nixon, M. S. (2002). Super-resolution land cover pattern prediction using a Hopfield neural network. *Remote Sensing of Environment*, 79, 1–14.

Tolpekin V. A., & Stein, A. (2009). Quantification of the effects of land-cover-class spectral separability on the accuracy of Markov-random-field based superresolution mapping. *IEEE Transactions on Geoscience and remote sensing*, 47, 3283–3297.

Tong, X., Xu, X., Plaza, A., Xie, H., Pan, H., Cao, W., Lv, D. (2016). A new genetic method for subpixel mapping using hyperspectral images. *IEEE Journal of Selected Topics in Applied Earth Observations and Remote Sensing*, 9, 4480–4491.

Townshend, R. G., Huang, C., Kalluri, S. N. V., Defries, R. S., Liang, S. (2000). Beware of per-pixel characterization of land cover. *International Journal of Remote Sensing*, 21, 839–843.

Van der Meer, F. D. (2012). Remote-sensing image analysis and geostatistics. *International Journal of Remote Sensing*, vol. 33, no. 18, pp. 5644–5676, 2012.

Verhoeye, J., & Wulf, R. De (2002). Land-cover mapping at sub-pixel scales using linear optimization techniques. *Remote Sensing of Environment*, 79, 96–104.

Villa, A., Chanussot, J., Benediktsson, J. A., Jutten, C. (2011). Spectral unmixing for the classification of hyperspectral images at a finer spatial resolution. *IEEE Journal of selected topics in signal processing*, 5, 521–533.

Wang, Q., Wang, L., Liu, D. (2012). Particle swarm optimization-based sub-pixel mapping for remote-sensing imagery. *International Journal of Remote Sensing*, 33, 6480–6496.

Wang, Q., Shi, W., Atkinson, P. M. (2014a). Sub-pixel mapping of remote sensing images based on radial basis function interpolation. *ISPRS Journal of Photogrammetry and Remote Sensing*, 92, 1–15.

671   Wang, Q., Shi, W., Wang, L. (2014b). Allocating classes for soft-then-hard subpixel mapping algorithms in units of class. *IEEE*

672   *Transactions on Geoscience and Remote Sensing*, 52, 2940–2959.

673   Wang, Q., Shi, W., Atkinson, P. M., Zhao, Y. (2015). Downscaling MODIS images with area-to-point regression kriging. *Remote*

674   *Sensing of Environment*, 166, 191–204.

675   Wang, Q., Shi, W., Atkinson, P. M. (2016). Spatial-temporal sub-pixel mapping of time-series images. *IEEE Transactions on*

676   *Geoscience and Remote Sensing*, 54, 5397–5411.

677   Wenny, B. N., Helder, D., Hong, J., Leigh, L., Thome, K. J., Reuter, D. (2015). Pre- and post-launch spatial quality of the Landsat 8

678   Thermal Infrared Sensor. *Remote Sensing*, 7, 1962–1980.

679   Xu, X., Zhong, Y., Zhang, L. (2014). A sub-pixel mapping method based on an attraction model for multiple shifted remotely sensed

680   images. *Neurocomputing*, 134, 79–91.

681   Xu, Y., & Huang, B. (2014). A spatio–temporal pixel-swapping algorithm for subpixel land cover mapping. *IEEE Geoscience and*

682   *Remote Sensing Letters*, 11, 474–478.

683   Zhang, L., Wu, K., Zhong, Y., Li, P. (2008). A new sub-pixel mapping algorithm based on a BP neural network with an observation

684   model. *Neurocomputing*, 71, 2046–2054.

685   Zhang, Y., Du, Y., Ling, F., Fang S., Li, X. (2014). Example-based super-resolution land cover mapping using support vector

686   regression. *IEEE Journal of Selected Topics in Applied Earth Observations and Remote Sensing*, 7, 1271–1283.

687   Zhang, Y., Du, Y., Ling, F., Li, X. (2015). Improvement of the example-regression-based super-resolution land cover mapping

688   algorithm. *IEEE Geoscience and Remote Sensing Letters*, 12, 1740–1744.

689   Zhong, Y., Wu, Y., Zhang, L., Xu, X. (2014). Adaptive MAP sub-pixel mapping model based on regularization curve for multiple

690   shifted hyperspectral imagery. *ISPRS Journal of Photogrammetry and Remote Sensing*, 96, 134–148.

691   Zhong, Y., Wu, Y., Xu, X., Zhang, L. (2015). An adaptive subpixel mapping method based on MAP model and class determination

692   strategy for hyperspectral remote sensing imagery. *IEEE Transactions on Geoscience and Remote Sensing*, 53, 1411–1426.

693